Catch bond drives stator mechanosensitivity in the bacterial flagellar motor

Ashley L Nord[a], Emilie Gachon[a], Ruben Perez-Carrasco[b], Jasmine A. Nirody[c], Alessandro Barducci[a], Richard M. Berry[d], and Francesco Pedaci[a,1]

[a]Centre de Biochimie Structurale (CBS), INSERM, CNRS, Université de Montpellier, 34090 Montpellier, France; [b]Department of Mathematics, University College London, London WC1E 6BT, United Kingdom; [c]Biophysics Graduate Group, University of California, Berkeley, CA 94720; and [d]Department of Physics, Clarendon Laboratory, University of Oxford, Oxford OX1 2JD, United Kingdom

Edited by Steven M. Block, Stanford University, Stanford, CA, and approved October 27, 2017 (received for review September 11, 2017)

The bacterial flagellar motor (BFM) is the rotary motor that rotates each bacterial flagellum, powering the swimming and swarming of many motile bacteria. The torque is provided by stator units, ion motive force-powered ion channels known to assemble and disassemble dynamically in the BFM. This turnover is mechanosensitive, with the number of engaged units dependent on the viscous load experienced by the motor through the flagellum. However, the molecular mechanism driving BFM mechanosensitivity is unknown. Here, we directly measure the kinetics of arrival and departure of the stator units in individual motors via analysis of high-resolution recordings of motor speed, while dynamically varying the load on the motor via external magnetic torque. The kinetic rates obtained, robust with respect to the details of the applied adsorption model, indicate that the lifetime of an assembled stator unit increases when a higher force is applied to its anchoring point in the cell wall. This provides strong evidence that a catch bond (a bond strengthened instead of weakened by force) drives mechanosensitivity of the flagellar motor complex. These results add the BFM to a short, but growing, list of systems demonstrating catch bonds, suggesting that this "molecular strategy" is a widespread mechanism to sense and respond to mechanical stress. We propose that force-enhanced stator adhesion allows the cell to adapt to a heterogeneous environmental viscosity and may ultimately play a role in surface-sensing during swarming and biofilm formation.

bacterial flagellar motor | molecular motor | mechanosensitivity | catch bond | *Escherichia coli*

The bacterial flagellar motor (BFM) is a large molecular complex found in many species of motile bacteria which actively rotates each flagellum of the cell, enabling swimming, chemotaxis, and swarming (1, 2). The rotor of the BFM is embedded within and spans the cellular membranes, coupling rotation to the extracellular hook and flagellar filament. Multiple transmembrane complexes, called stator units, are anchored around the perimeter of the rotor and bound to the rigid peptidoglycan (PG) layer (3–5). By harnessing the ion motive force, the stator units are responsible for torque generation, acting upon the common ring formed by FliG proteins on the cytosolic side of the rotor (Fig. 1*A*) (6, 7).

Several studies have revealed the continuous exchange of various BFM molecular constituents (8–10), demonstrating that a static model for the BFM structure is not adequate. A prime example, and in contrast to macroscopic rotary motors, the stator of the BFM is dynamic; while each bound stator unit acts upon the rotor independently (11, 12), their stoichiometry in the motor varies. Once anchored around the rotor, stator units dynamically turn over, eventually diffusing away in the inner membrane (10). Each additional recruited stator unit increases the total torque and thus the measured rotational speed of the motor (11, 13), and up to 11 units have been observed to engage in an individual motor in *Escherichia coli* (10, 14–16).

Recently, novel observations revealed that the stator units are also mechanosensors (17–19). A variety of mechanosensitive membrane protein complexes exist in all three kingdoms of life (20). Although these complexes vary widely in their structure, function, and sensitivity, they share one key feature: The conformational state, and thus the function, of the protein is directly dependent upon mechanical stress, mediated by the surrounding cell membrane. Two recent works have shown that stator recruitment in the BFM depends on the viscous load placed upon the motor (17, 18). The property of mechanosensing (likely relevant for the cell to overcome local inhomogeneities and obstacles) has important consequences for the interpretation of previous data and ultimately for successfully modeling the torque generation of the BFM. It implies, in fact, that previously measured torque–speed relationships (11, 21–23) are likely composed of motors with a dynamically changing number of stator units. Theoretical models must now take this novel fact into consideration (12).

Here, to better elucidate the molecular mechanism responsible for the mechanosensitivity of the BFM, we investigate single motors and quantify stator stoichiometry. Using an external magnetic field and magnetic microbeads of different sizes bound to the hook of individual *E. coli* motors, we rapidly manipulate the load experienced by the motor by reversibly stalling its rotation. The external load manipulation directly probes the mechanosensitivity of the BFM: We stimulate stator binding during the period of stall and observe and quantify stator unbinding after release. We perform these experiments for various viscous loads, each of which imposes a different initial stator occupancy. This allows us to statistically characterize the kinetics of stator stoichiometry both in steady-state conditions and following a rapid change in external load. Our analysis suggests that a catch-bond mechanism (a bond counterintuitively strengthened, instead of weakened, by force) (24–26) is at the heart of

Significance

The bacterial flagellar motor (BFM) is the rotary motor powering swimming of many motile bacteria. Many of the components of this molecular machine are dynamic, a property which allows the cell to optimize its behavior in accordance with the surrounding environment. A prime example is the stator unit, a membrane-bound ion channel that is responsible for applying torque to the rotor. The stator units are mechanosensitive, with the number of engaged units dependent on the viscous load on the motor. We measure the kinetics of the stators as a function of the viscous load and find that the mechanosensitivity of the BFM is governed by a catch bond: a counterintuitive type of bond that becomes stronger under force.

Author contributions: A.L.N. and F.P. designed research; A.L.N. and E.G. performed research; R.P.-C. contributed new reagents/analytic tools; A.L.N., R.P.-C., J.A.N., A.B., R.M.B., and F.P. analyzed data; and A.L.N., R.M.B., and F.P. wrote the paper.

The authors declare no conflict of interest.

This article is a PNAS Direct Submission.

[1]To whom correspondence should be addressed. Email: francesco.pedaci@cbs.cnrs.fr.

This article contains supporting information online at www.pnas.org/lookup/suppl/doi:10.1073/pnas.1716002114/-/DCSupplemental.

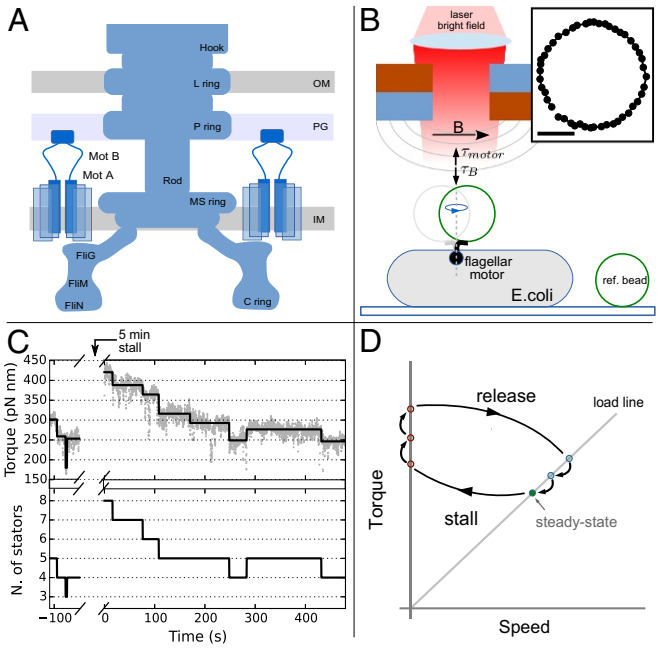

Fig. 1. The experimental assay. (*A*) Schematic of the BFM showing rotor and stator protein complexes. Stator units bind to the PG at the periphery of the rotor, providing torque via an interaction with FliG. IM, inner membrane; OM, outer membrane. (*B*) Experimental setup. Bacterial cells are immobilized onto a coverslip, and a rotating superparamagnetic bead attached to the hook of a BFM is imaged and tracked. Two permanent magnets (mounted on a vertical translation stage) create a magnetic field, capable of generating sufficient torque τ_B on the bead to stall the motor. Ref., reference. (*B*, *Inset*) Tracked positions of a 1μm bead rotating one turn. (Scale bar: 100 nm.) (*C*) One experimental trace. Motor torque (*C*, *Upper*; gray points) is measured before stall ($t < 0$), then again immediately upon release ($t > 0$). The output of the step detection algorithm (black line) is used to determine stator stoichiometry (*C*, *Lower*). N., number. (*D*) The experimental assay shown in the torque speed plane, where stators may associate during 5-min motor stall, subsequently dissociating back to steady-state occupancy after stall (points in red not directly observed).

BFM mechanosensitity, dynamically remodeling stator stoichiometry against changes in external resistance to rotation.

Results

Torque Measurement and Load Manipulation. A nonswitching strain of *E. coli* lacking flagellar filaments and containing an endogenously biotinylated hook (27) is used for all experiments. Streptavidin-coated superparamagnetic beads are attached to the hook of cells immobilized on a coverslip, and the rotation of the beads is observed via wide-field holographic microscopy (28) (Fig. 1*B*). Tracking the position of the bead in time, we calculate the velocity and torque, as described in *Materials and Methods*. Data are acquired for motors driving five different viscous loads, which are obtained by using beads of three different diameters and two buffer solutions of different viscosity, as indicated in Table S1 (see *SI Materials and Methods* for details). Two permanent magnets are mounted, as shown in Fig. 1*B*. The magnets are attached to a motorized vertical translation stage which controls the distance between the magnets and the sample, and thus the magnitude of the magnetic field at the sample plane. Both the BFM and the magnetic field exert a torque on the magnetic bead. For sufficiently large magnetic fields, the bead, and thus the motor, remain stalled in an equilibrium angular position, where the magnetic torque and the motor torque cancel (29).

For a given bead size, the steady-state rotation of individual motors is measured under a negligible magnetic field for 50–300 s before manipulation. The magnets are then lowered until the magnetic torque stalls the motor rotation, and the motor is held at stall for 300 s. The magnets are then raised to the original height; the load is returned to that supplied by the bead in its viscous environment; and the rotation of the motor is recorded for at least another 5 min. Each movement of the magnets occurs within 3 s. The load felt by the BFM is therefore quickly and dynamically manipulated twice during the measurement of an individual motor; an exemplification of this procedure is shown in the torque–speed plane in Fig. 1*D*. The torque of individual motors is measured first at steady state before stall and then again immediately after stall. An example torque trace for the viscous load γ_{500} is shown in Fig. 1 *C*, *Upper* (see also Fig. S1 for a collection of individual traces at different viscous loads). An increase in torque during stall is evident, followed by a stepwise relaxation to a torque value close to the original steady-state value.

Viscous Load Dependency of Stator Assembly Dynamics. Under the assumption that torque traces represent noisy constant signals demarcated by discrete discontinuities due to stator association or dissociation, we use a recently developed step-detection algorithm (30, 31) to fit the individual torque traces. By using this fit, a developed algorithm (*Materials and Methods* and *SI Materials and Methods*) is used to calculate stator stoichiometry, extracting stator number as a function of time, $N(t)$, for each individual trace. Contrary to previous works, this algorithm determines stator stoichiometry based upon the discrete discontinuities of the torque traces, not upon the absolute value of the torque; given the broad distributions of single-stator torque values (Fig. 2*A*), this approach greatly reduces the error in stator stoichiometry estimation. Simulations (Fig. S2) suggest that, given the average noise in our torque measurements, the algorithms used here reconstructs the stator stoichiometry with an accuracy of 1.6 stator units and that the shortest states in stator stoichiometry, which can be reliably resolved, last 3.5 s.

In Fig. 2, we show distributions and average time courses of the number of stator units $N(t)$ in multiple repeats of the procedure illustrated in Fig. 1. From the change in torque produced by stator association and dissociation events, we quantify the distribution of torque produced by a single-stator unit (Fig. 2*A*). This analysis shows that the torque generated by a single-stator unit increases with increasing viscous load (and decreasing speed), matching theoretical models of stator behavior (12, 32). This finding is in agreement with previous results based on sodium-driven PomAB stator units (33), confirming that MotAB stator units behave in a similar manner. Additionally, at steady state, we observe that the average stator occupancy increases with increasing applied viscous load (Fig. 2*B* and Fig. S3); this dependency is the fingerprint of stator mechanosensitivity.

In Fig. 2*C*, we show for each viscous load the average (colored line) and SD (shaded region) of the number of stator units $N(t)$ obtained from different motors, before and after stall. For all of the viscous loads except for the highest (γ_{1300}), the average stator number increases during stall. This is quantified in Fig. 2*D*: Stalling a viscous load γ_{1300} for 300 s does not yield a relevant change in stator number (-0.3 ± 1.1), while for the other viscous loads, mechanosensing causes the recruitment of additional stator units during stall (1.0 ± 1.3 for γ_{500g}, 1.7 ± 1.1 for γ_{500}, 2.0 ± 1.4 for γ_{300g}, and 2.3 ± 1.8 for γ_{300}). After stall, as visible in Fig. 2*C*, $N(t)$ decays back to the prestall, steady-state value within $\sim 200 - 300$ s. This implies that, on average, for all of the viscous loads except for the largest, additional stator units bind and engage with the BFM during the 300 s the motor is stalled. Within minutes after the magnetic field is removed and rotation resumed under the original viscous load, stator units dissociate, and their average number returns to the previous steady-state value, which depends on the viscous load experienced during rotation. This behavior is not observed at the highest viscous load γ_{1300}, which shows, on average, the same torque after stall as before, indicating that no statistically relevant change in stator number occurs during stall for this high viscous load.

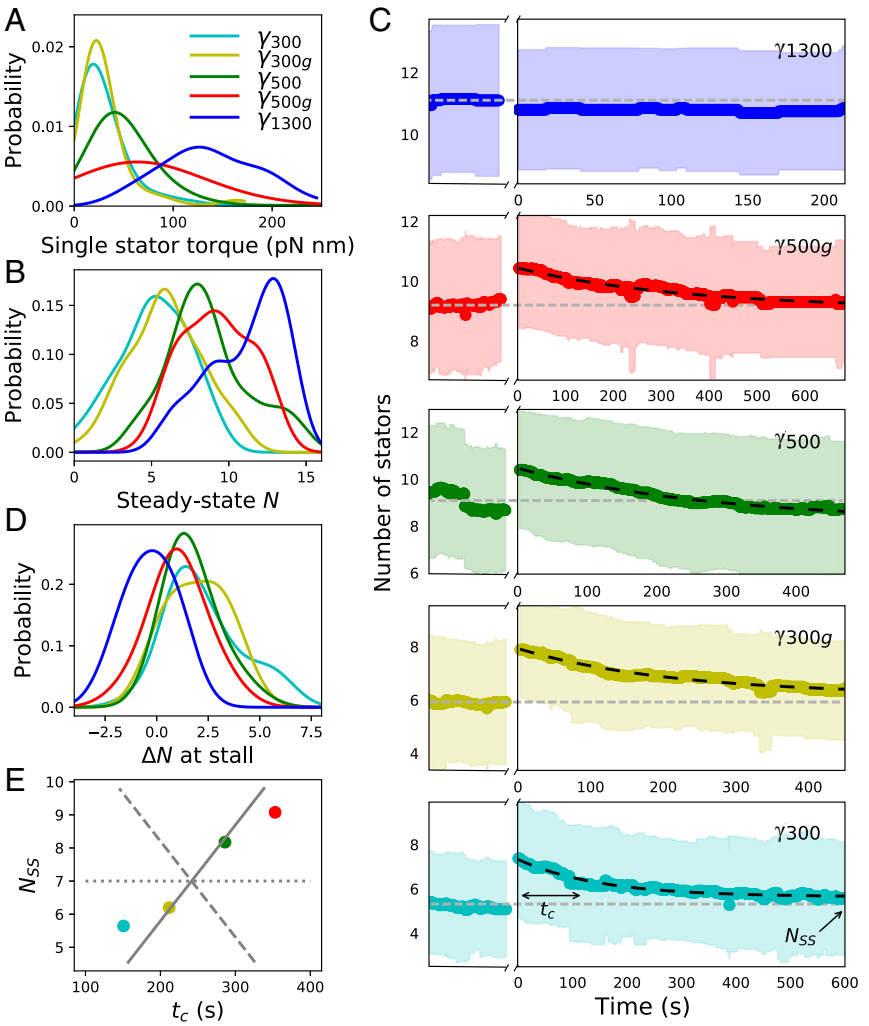

Fig. 2. Stator stoichiometry before and after stall. (*A* and *B*) Kernel density estimates (KDEs) of the single-stator torque contribution and the steady-state stoichiometry, respectively, as a function of external viscous load. (*C*) Temporal evolution of stator stoichiometry of motors driving the different viscous loads (color-coded as in *A*, *B*, *D*, and *E*). Steady-state rotation of the viscous load corresponds to time $t < 0$. The motor is then stalled by the magnetic field for a period of 300 s (indicated by a break in the *x* axis). At $t = 0$, the motor is released from stall. The thick color-coded line and the colored region are the average and SD of multiple motors. The horizontal gray dashed line indicates the average number of stator units measured for $t < 0$ at steady state. The dark dashed line is the fit obtained from Eq. **3** for $t > 0$. N_{SS} and t_c in the bottom image indicate the parameters extracted by the exponential fit using Eq. **3**. (*D*) KDE of the number of stator units recruited during stall as a function of external viscous load. (*E*) Steady-state stoichiometry, N_{ss}, as a function of the characteristic relaxation time, t_c. For comparison, gray lines show the predictions of models, where the variation in K_D is due entirely to k_{on} (dashed), entirely to k_{off} (solid), or split equally between k_{on} and k_{off} (dotted). Number of motors analyzed was 24 for γ_{300}, 28 for γ_{300g}, 40 for γ_{500}, 30 for γ_{500g}, and 20 for γ_{1300}.

Modeling Stator Assembly Dynamics. To determine the stator binding and unbinding rates, a model of stator assembly is required. The simplest model of stator assembly kinetics, previously used implicitly (10, 34), could be written as a Hill–Langmuir adsorption model (35). This model describes the rotor as surrounded by N_{max} independent and noninteracting binding sites. A diffusing stator unit can bind to an empty site with a rate constant k_{on}, while a bound stator unit can disengage with a rate constant k_{off}. The resulting average stator occupancy $N(t)$ follows the dynamics

$$\frac{dN}{dt} = k_{on}(N_{max} - N) - k_{off}N. \qquad [1]$$

Here, the concentration of unbound stator units is considered constant and unaffected by the binding and unbinding events. At steady state, $dN/dt = 0$, and the steady-state stator occupancy, N_{ss}, is determined by

$$N_{ss} = \frac{N_{max}}{1 + K_D}. \qquad [2]$$

where $K_D = k_{off}/k_{on}$ is the dissociation constant. Under steady-state conditions, previous observations of stator turnover (10) can be explained by the reestablishment of the steady-state number of stator units against fluctuations. This model is analogous to reversible random sequential adsorption (RSA) models (36, 37); in this case, the discrete lattice takes the form of a circle at the periphery of the rotor, and each unit occupies one lattice site.

In line with published experiments demonstrating stator mechanosensing (17, 18), the viscous load-dependent distributions of $N(t)$ that we measure under steady-state conditions, N_{ss}, shown in Fig. 2*B*, show that K_D decreases with increasing viscous load. Rapidly stalling a motor is equivalent to switching its viscous load to infinite ($\gamma \to \infty$) and has the effect of increasing N_{ss}. Accordingly, in our experiments, except for the viscous load γ_{1300}, we observe a clear increase in the number of stator units after stall, indicating stator assembly upon an increase in

applied load. A load-dependent K_D indicates a load dependence in either or both of k_{on} and k_{off}.

To investigate this further, we analyze the relaxation traces by comparing them with the analytical solution of Eq. **1**, which predicts an exponential decay toward the steady-state occupancy N_{ss},

$$N(t) = N_{ss} + (N_o - N_{ss})e^{-(k_{on}+k_{off})t}, \quad [3]$$

where N_o is the observed stator occupancy after the stall ($t = 0$). The experimental mean traces for $N(t)$ after stall, shown in Fig. 2*C*, are well fit by a single exponential (dashed lines); this simple model of stator binding kinetics is thus compelling, and it allows the estimation of the binding and unbinding rates from the experimental traces using Eq. **1**. Defining $t_c = 1/(k_{on} + k_{off})$ as the fitted decay time in figure Fig. 2*C*, in combination with Eq. **2**, we find

$$k_{on} = \frac{N_{ss}}{t_c N_{max}}, \quad [4]$$

$$k_{off} = \frac{N_{max} - N_{ss}}{t_c N_{max}}. \quad [5]$$

Fig. 2*E* plots experimental fits for N_{ss} and t_c against each other (circles) and compares predictions of models where the variation in K_D is due entirely to k_{on} (dashed line), entirely to k_{off} (solid line), or split equally between k_{on} and k_{off} (dotted line). Fig. 3*A* shows k_{on} and k_{off} from Eqs. **4** and **5** vs. viscous load. It is evident that the differences in relaxation after stall are mainly due to a change in k_{off} with viscous load, while k_{on} is relatively independent of load. For the highest viscous load γ_{1300}, we find that N does not change during stall and the exponential relaxation is absent (Fig. 2*C*), so the rates cannot be extracted. This suggests that $K_D(\gamma_{1300}) \sim K_D(\gamma = \infty)$, i.e., that the BFM mechanosensitivity saturates for high loads $\gamma \geq \gamma_{1300}$, and that there is no dynamical difference between rotating such a high viscous load and being stalled. To quantify the rates at γ_{1300}, given the relatively constant value of k_{on} for the smaller viscous loads, we make the assumption that $k_{on}(\gamma_{1300})$ is equal to the average of k_{on} for the smaller loads. From the value of $N_{ss}(\gamma_{1300})$, we can then obtain $k_{off}(\gamma_{1300})$ from Eq. **2**.

While the proposed Hill–Langmuir adsorption model is sufficient to explain and fit our experimental data, we note that there is no evidence for fixed binding sites at the periphery of the rotor in *E. coli*. Therefore, we also explore a more generalized reversible RSA model which resembles the classic "car parking problem" (36, 37), where the stator binding is not restricted to a discrete number of binding sites, but can occur continuously at any angular position on the ring (Fig. S4 *A* and *B*). In this model, a new stator unit cannot bind unless enough contiguous space is available in the ring (overlap is not allowed), which depends on the positions of the units currently bound. Hence, memory effects due to excluded volume arise, affecting the stator occupancy dynamics, $N(t)$. The details of this model are further discussed in *SI Materials and Methods*. Numerical simulations of the model (*Materials and Methods* and *SI Materials and Methods*) exhibit similar relaxation dynamics to the experiments and the Hill–Langmuir model, and we conclude that both models can adequately fit our experimental observations. Strikingly, the extracted rates from fits of the experimental data are very similar to those of the Hill–Langmuir model (Fig. S4*C*), confirming the viscous load-independent binding probability combined with an unbinding probability that decreases for increasing viscous loads.

Discussion

In this study, we directly probe BFM mechanosensing behavior, providing an extensive quantification of stator stoichiometry as a function of external viscous load, both at steady state and immediately after a controlled change of load. By fitting measured stator kinetics to a reversible RSA model, we provide a measurement of stator association and dissociation rates as a function of external viscous load.

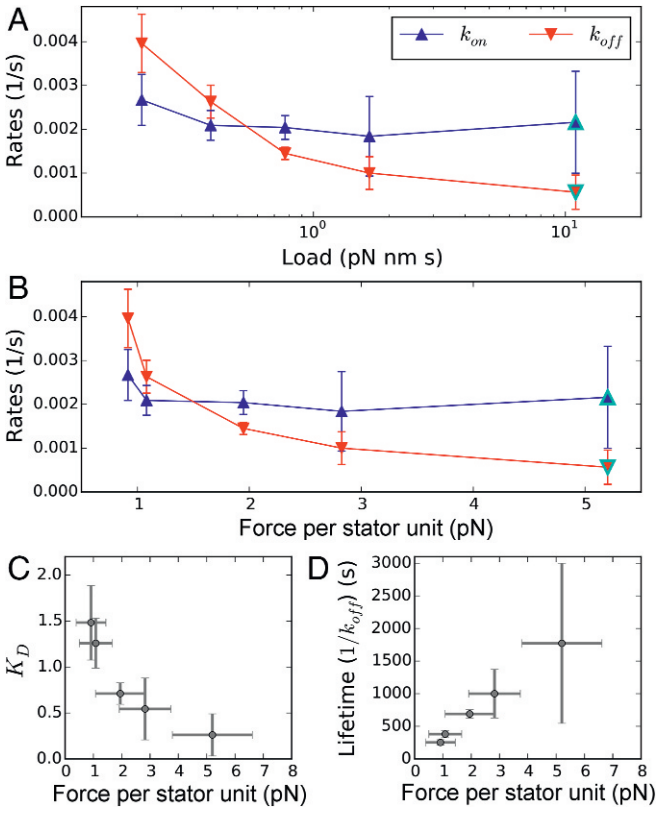

Fig. 3. Stator kinetics. (*A* and *B*) The binding and unbinding rates of the stator units as a function of external viscous load on the motor (*A*) and single-stator force (*B*). All rates are calculated by fitting Eq. **3** to traces in Fig. 2*C*, with the exception of points outlined in cyan (*SI Materials and Methods*). (*C* and *D*) Dissociation constant, K_D, and lifetime of an individual stator in the motor complex, respectively, as a function of the average local force applied by a single stator to the rotor (and by symmetry to the PG layer). Points and error bars give averages and standard deviations, respectively.

Stator unit mechanosensitivity must arise from a load dependence in one or both of the stator association and dissociation rates. It has been suggested that force upon the PG may cause structural changes in stator binding sites which may affect stator unit association rate (17). Additionally, crystal structures of $MotB_C$ of *Salmonella* and $PomB_C$ of *Vibrio* suggest that a drastic conformational change in the N-terminal portion of $MotB_C/PomB_C$ is required for the stator to bind to the PG (38, 39). Mutational studies suggest that this conformational change may be triggered by an interaction between the cytoplasmic domain of MotA and FliG (40), a process potentially complicated by the rotation of the rotor. Thus, one might imagine that the rate of stator unit association could be dependent upon the speed of the motor. However, we find that the rate of stator association is independent of viscous load, while the rate of stator dissociation is load-dependent, and it is in fact this property that begets mechanosensitivity in the BFM.

Fig. 2*B* shows our measurements of N_{ss} as a function of viscous load, confirming previous results (17, 18) that steady-state stator number is proportional to viscous load. The saturation curve of this relationship (Fig. S3) is consistent with previous measurements of motor fluorescence as a function of viscous load (where the signal of fluorescent fusion stator units was a proxy for stator number) (18). While this work provides evidence for a load-dependent K_D, it is unable to determine whether this dependence is governed by k_{on}, k_{off}, or both. A previous measurement of k_{off} (10), performed on immobilized cells where motors were

presumably stalled via the attachment of flagella to the coverslip, reported a value two orders of magnitude faster than our measured $k_{off}(\gamma_{1300})$. However, this study was performed with stator units fused to a fluorescent protein, which can cause different behaviors from their wild-type counterparts (10, 41). The present study reports on the dynamics of wild-type stator units in otherwise unperturbed motors.

Interestingly, our quantification of the viscous load dependence of stator association and dissociation rates has an important consequence for the molecular mechanism responsible for stator mechanosensitivity in the BFM. We see that an increase in external viscous load translates into a higher torque exerted by each stator unit on the rotor (Fig. 2*A*). Considering the average single-unit torque and the radius of the rotor [23 nm (42)], we quantify the mean local force applied by each single unit onto the rotor (found in the range of few piconewtons; Fig. 3*B*). We note that, by reaction, this is also the force with which the unit simultaneously pulls upon and stretches its connection to the PG. In Fig. 3 *C* and *D*, we show the measured dissociation constant K_D and lifetime $(1/k_{off})$ of the stator units as a function of this force. This counterintuitive relationship is the canonical fingerprint of catch-bond behavior (24–26). While the lifetime of a conventional slip bond decreases if tension is applied across it, a catch bond produces a maximum of the lifetime at a nonzero force. A hook under tension and a children's finger trap are two macroscopic analogies of this nontrivial molecular mechanism. We therefore conclude that the kinetic rates we measure suggest the existence of a catch bond in the anchoring region of the stator on the PG. We predict that if a force greater than the maximum force generated by a single unit could be applied to the anchor of the stator unit to the PG, the catch-bond behavior will eventually transform into slip-bond behavior, as observed in other biological catch bonds (25, 43).

The interface between the PG and the MotB PG-binding (PGB) domain, located at the C-terminal of MotB ($MotB_C$), is where the force can have an impact on the bonds relevant for the lifetime of the stator unit around the rotor. While our data indicate a catch-bond mechanism, they cannot discriminate any structural detail. However, interestingly, it has been reported that the putative key PGB residues in the structure of the PGB dimer of MotB are buried and not readily accessible (44) and that a substantial structural flexibility of the domain is considered necessary to mask and unmask them (45). The N-terminal portion of MotB must perform a large conformational extension to reach the PG (38, 39). Recently, a conformational change upon binding has also been hypothesized in the PG-associated C-terminal of the closely related Outer Membrane protein OmpA (46). These facts suggest a possible catch-bond mechanism in which tension across the PG–$MotB_C$ interface can promote either conformational rearrangements or a positional shift of the PGB within the PGB pocket which lead to further exposure of binding residues to the PG, increasing the strength of the bond and the lifetime of the stator unit within the BFM complex (as sketched in Fig. 4). While multiple multidimensional and one-dimensional phenomenological models exist to explain catch bonds, further knowledge of the structure or multidimensional energy landscape of the unbinding pathway will be required to extract physically relevant parameters describing the $MotB_C$–PG interaction (47).

As single-molecule spectroscopy techniques continue to develop, the prevalence of experimental data demonstrating biological catch bonds grows. Catch bonds have already been shown to play an important role for two other molecular motors, myosin (48) and dynein (49, 50). Here, we suggest that the mechanosensitivity of the BFM may also be explained by a catch-bond mechanism within the stator. This feature potentially allows the cell to replace damaged stator units, adapt to the prevailing environmental viscosity, and avoid wasting energy during flagellar growth, and may also play a role in behaviors which require surface-sensing, such as swarming motility and biofilm formation. The wild-type *E. coli* motor is bidirectional, and previous

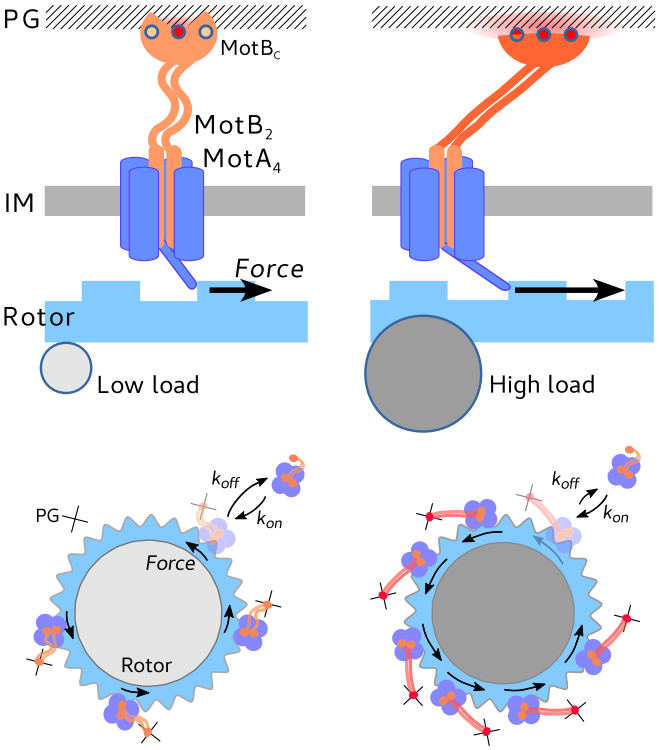

Fig. 4. Cartoon of a proposed catch-bond mechanism. The average force produced by the stator upon the rotor (blue arrow) stretches the stator anchoring point at the PG, inducing either conformational changes or a positional shift of the PGB within the PGB pocket that increase the bond strength and lifetime. The average force is higher for a larger viscous load (*Right*), with respect to a low viscous load (*Left*), as shown in Fig. 2*A*, and consistent with previously published torque–speed curves. IM, inner membrane.

results show that stator assembly is dependent upon load for both counterclockwise- and clockwise-locked motors (17, 18). While catch bonds are often directional or asymmetrically directional (51), the catch-bond behavior of the stator may prove to be symmetrically bidirectional. Finally, FliL is a membrane protein which associates with the stator and rotor, although its exact function is still poorly defined (17, 52–54). The potential role of FliL with respect to the stator's mechanosensitivity remains to be discovered.

Materials and Methods

Extended materials and methods are included in *SI Materials and Methods*.

Bacteria and Experimental Configuration. We use *E. coli* strain MTB32, which has a biotinylated hook (27), and we additionally genetically delete *CheY*. Frozen aliquots of cells are grown in Terrific Broth at 33 °C for 5 h, shaking at 200 rpm, to a final OD_{600} of 0.5–0.6. Cells are immobilized to a poly-L-lysine–coated coverslip in custom-made flow slides. Streptavidin superparamagnetic beads are allowed to spontaneously attach to the biotinylated hooks. Experiments are performed in motility buffer at 22 °C.

Rotating beads are imaged onto a CMOS camera at 1,000 Hz and localized by using cross-correlation analysis (28, 55). An ellipse is fit to the bead positions to yield the angular positions. An example trajectory is shown in Fig. 1 *B*, *Inset*. Speed traces are median-filtered by using a window of 0.5 s. Two magnets are mounted onto a linear motor above the sample plane (56).

Motor Torque Calculation and Fitting. The torque of the BFM is calculated as $\tau_{motor} = \gamma\omega$, where γ is the rotational viscous drag coefficient of the bead (57), and ω is the measured rotational velocity. Torque traces are assumed to be noisy piecewise constant signals, and a minimization of the L^1-Potts functional is used to fit both the prestall and poststall motor torque traces. This is done via the PottsLab toolbox (Version 0.42) in Matlab (31, 58). An example torque trace and its fit is shown in Fig. 1*C*.

Stator Stoichiometry Calculation and Analysis. Stator stoichiometry is determined by preserving the discrete discontinuities from the step detection algorithm (see *SI Materials and Methods* for details and a test of both the step detection and stator stoichiometry determination algorithms).

Numerical Simulations. In addition to the Hill–Langmuir adsorption model described by Eq. **3**, we also consider a generalized reversible RSA model which incorporates a continuous binding ring around the rotor. As this model has no analytical solution, we determine stator binding and unbinding rates using a genetic algorithm (differential evolution) to match simulated stator stoichiometry time trajectories to the average of the experimental trajectories.

ACKNOWLEDGMENTS. We thank H. J. E. Beaumont and D. Dulin for constructive comments; D. Chamousset for technical help; and M. Storath and A. Weinmann for step detection algorithms and support in implementation. Centre de Biochimie Stucturale is a member of the France-BioImaging and the French Infrastructure for Integrated Structural Biology, supported by Grants ANR-10-INBS-04-01 and ANR-10-INBS-05. R.P.-C. was supported by Wellcome Trust Grant WT098325MA, and A.L.N., E.G., and F.P. were supported by the European Research Council under the European Union's Seventh Framework Program (FP/2007-2013)/ERC Grant 306475. A.B. acknowledges the support of the French Agence Nationale de la Recherche, under Grant ANR-14-ACHN-0016.

1. Sowa Y, Berry RM (2008) Bacterial flagellar motor. *Quart Rev Biophys* 41:103–132.
2. Minamino T, Imada K, Namba K (2008) Molecular motors of the bacterial flagella. *Curr Opin Struct Biol* 18:693–701.
3. De Mot R, Vanderleyden J (1994) The C-terminal sequence conservation between OmpA-related outer membrane proteins and MotB suggests a common function in both gram-positive and gram-negative bacteria, possibly in the interaction of these domains with peptidoglycan. *Mol Microbiol* 12:333–334.
4. Chun SY, Parkinson JS (1988) Bacterial motility: Membrane topology of the Escherichia coli MotB protein. *Science* 239:276–278.
5. Hizukuri Y, Morton JF, Yakushi T, Kojima S, Homma M (2009) The peptidoglycan-binding (PGB) domain of the Escherichia coli pal protein can also function as the PGB domain in *E. coli* flagellar motor protein MotB. *J Biochem* 146:219–29.
6. Kim EA, Price-Carter M, Carlquist WC, Blair DF (2008) Membrane segment organization in the stator complex of the flagellar motor: Implications for proton flow and proton-induced conformational change. *Biochem.* 47:11332–11339.
7. Kojima S, Blair DF (2001) Conformational change in the stator of the bacterial flagellar motor. *Biochemistry* 40:13041–13050.
8. Delalez NJ, et al. (2010) Signal-dependent turnover of the bacterial flagellar switch protein FliM. *Proc Natl Acad Sci USA* 107:11347–11351.
9. Delalez NJ, Berry RM, Armitage JP (2014) Stoichiometry and turnover of the bacterial flagellar switch protein FliN. *mBio* 5:e01216-14.
10. Leake MC, et al. (2006) Stoichiometry and turnover in single, functioning membrane protein complexes. *Nature* 443:355–358.
11. Ryu WS, Berry RM, Berg HC (2000) Torque-generating units of the flagellar motor of *Escherichia coli* have a high duty ratio. *Nature* 403:444–447.
12. Nirody J, Berry R, Oster G (2016) The limiting speed of the bacterial flagellar motor. *Biophys J* 111:557–564.
13. Blair DF, Berg HC (1988) Restoration of torque in defective flagellar motors. *Science* 242:1678–1681.
14. Reid SW, et al. (2006) The maximum number of torque-generating units in the flagellar motor of *Escherichia coli* is at least 11. *Proc Natl Acad Sci USA* 103:8066–8071.
15. Samuel AD, Berg HC (1996) Torque-generating units of the bacterial flagellar motor step independently. *Biophys J* 71:918–923.
16. Khan S, Dapice M, Reese TS (1988) Effects of mot gene expression on the structure of the flagellar motor. *J Mol Biol* 202:575–584.
17. Lele PP, Hosu BG, Berg HC (2013) Dynamics of mechanosensing in the bacterial flagellar motor. *Proc Natl Acad Sci USA* 110:11839–11844.
18. Tipping MJ, Delalez NJ, Lim R, Berry RM, Armitage JP (2013) Load-dependent assembly of the bacterial flagellar motor. *mBio* 4:e00551-13.
19. Che YS, et al. (2014) Load-sensitive coupling of proton translocation and torque generation in the bacterial flagellar motor. *Mol Microbiol* 91175–184.
20. Kung C, Martinac B, Sukharev S (2010) Mechanosensitive channels in microbes. *Annu Rev Microbiol* 64:313–329.
21. Berg HC, Turner L (1993) Torque generated by the flagellar motor of *Escherichia coli*. *Biophys J* 65:2201–2216.
22. Berry RM, Berg HC (1999) Torque generated by the flagellar motor of *Escherichia coli* while driven backward. *Biophys J* 76:580–587.
23. Chen X, Berg HC (2000) Torque-speed relationship of the flagellar rotary motor of *Escherichia coli*. *Biophys J* 78:1036–1041.
24. Thomas W, Vogel V, Sokurenko E (2008) Biophysics of catch bonds. *Annu Rev Biophys* 37:399–416.
25. Sokurenko E, Vogel V, Thomas W (2008) Catch-bond mechanism of force-enhanced adhesion: Counterintuitive, elusive, but...widespread? *Cell Host Microbe* 16:314–323.
26. Prezhdo O, Pereverzev Y (2009) Theoretical aspects of the biological catch bond. *Acc Chem Res* 42:693–703.
27. Brown MT, et al. (2012) Flagellar hook flexibility is essential for bundle formation in swimming *Escherichia coli* cells. *J Bacteriol* 194:3495–3501.
28. Dulin D, Barland S, Hachair X, Pedaci F (2014) Efficient illumination for microsecond tracking microscopy. *PLoS One* 9:e107335.
29. van Oene MM, et al. (2015) Biological magnetometry: Torque on superparamagnetic beads in magnetic fields. *Phys Rev Lett* 114:218301.
30. Weinmann A, Storath M (2015) Iterative Potts and Blake–Zisserman minimization for the recovery of functions with discontinuities from indirect measurements. *Proc Roy Soc Lond Ser A Math Phys Sci* 471:20140638.
31. Storath M, Weinmann A, Demaret L (2014) Jump-sparse and sparse recovery using potts functionals. *IEEE Trans Signal Process* 62:3654–3666.
32. Mandadapu KK, Nirody JA, Berry RM, Oster G (2015) Mechanics of torque generation in the bacterial flagellar motor. *Proc Natl Acad Sci USA* 112:E4381–E4389.
33. Lo CJ, Sowa Y, Pilizota T, Berry RM (2013) Mechanism and kinetics of a sodium-driven bacterial flagellar motor. *Proc Natl Acad Sci USA* 28:E2544–E2551.
34. Tipping MJ, Steel BC, Delalez NJ, Berry RM, Armitage JP (2013) Quantification of flagellar motor stator dynamics through in vivo proton-motive force control. *Mol Microbiol* 87:338–347.
35. Foreman JC, Johansen T, Gibb AJ (2010) *Textbook of Receptor Pharmacology* (CRC, Boca Raton, FL).
36. Evans JW (1993) Random and cooperative sequential adsorption. *Rev Mod Phys* 65:1281–1329.
37. Lee JW (2004) Reversible random sequential adsorption on a one-dimensional lattice. *Physica A* 331:531–537.
38. Zhu S, et al. (2014) Conformational change in the periplamic region of the flagellar stator coupled with the assembly around the rotor. *Proc Natl Acad Sci USA* 111:13523–13528.
39. Kojima S, et al. (2009) Stator assembly and activation mechanism of the flagellar motor by the periplasmic region of motb. *Mol Microbiol* 73:710–718.
40. Kojima S, Nonoyama N, Takekawa N, Fukuoka H, Homma M (2011) Mutations targeting the C-terminal domain of FliG can disrupt motor assembly in the Na^+-driven flagella of vibrio alginolyticus. *J Mol Biol* 414:62–74.
41. Heo M, et al. (2017) Impact of fluorescent protein fusions on the bacterial flagellar motor. *Sci Rep* 7:12583.
42. DePamphilis ML, Adler J (1971) Fine structure and isolation of the hook-basal body complex of flagella from *Escherichia coli* and *Bacillus subtilis*. *J Bacteriol* 105:384–395.
43. Barsegov V, Thirumalai D (2005) Dynamics of unbinding of cell adhesion molecules: Transition from catch to slip bonds. *Proc Natl Acad Sci USA* 102:1835–1839.
44. Roujeinikova A (2008) Crystal structure of the cell wall anchor domain of MotB, a stator component of the bacterial flagellar motor: Implications for peptidoglycan recognition. *Proc Natl Acad Sci USA* 105:10348–10353.
45. Reboul CF, Andrews DA, Nahar MF, Buckle AM, Roujeinikova A (2011) Crystallographic and molecular dynamics analysis of loop motions unmasking the peptidoglycan-binding site in stator protein MotB of flagellar motor. *PLoS One* 6:e18981.
46. Tan K, et al. (2017) Insights into PG-binding, conformational change, and dimerization of the OmpA C-terminal domains from Salmonella enterica serovar Typhimurium and *Borrelia burgdorferi*. *Protein Sci* 26:1738–1748.
47. Chakrabarti S, Hinczewski M, Thirumalai D (2016) Phenomenological and microscopic theories for catch bonds. *J Struct Biol* 197:50–56.
48. Guo B, Guilford WH (2006) Mechanics of actomyosin bonds in different nucleotide states are tuned to muscle contraction. *Proc Natl Acad Sci USA* 103:9844–9849.
49. Leidel C, Longoria RA, Gutierrez FM, Shubeita GT (2012) Measuring molecular motor forces in vivo: Implications for tug-of-war models of bidirectional transport. *Biophys J* 103:492–500.
50. Rai AK, Rai A, Ramaiya AJ, Jha R, Mallik R (2013) Molecular adaptations allow dynein to generate large collective forces inside cells. *Cell* 152:172–182.
51. Huang DL, Bax NA, Buckley CD, Weis WI, Dunn AR (2017) Vinculin forms a directionally asymmetric catch bond with f-actin. *Science* 357:703–706.
52. Zhu S, Kumar A, Kojima S, Homma M (2015) FliL associates with the stator to support torque generation of the sodium-driven polar flagellar motor of vibrio. *Mol Microbiol* 98:101–110.
53. Partridge JD, Nieto V, Harshey RM (2015) A new player at the flagellar motor: FliL controls both motor output and bias. *mBio* 6:e02367-14.
54. Chawla R, Ford KM, Lele PP (2017) Torque, but not flil, regulates mechanosensitive flagellar motor-function. *Sci Rep* 7:5565.
55. Lipfert J, Kerssemakers JJW, Rojer M, Dekker NH (2011) A method to track rotational motion for use in single-molecule biophysics. *Rev Sci Instrum* 82:103707.
56. Lipfert J, Hao X, Dekker NH (2009) Quantitative modeling and optimization of magnetic tweezers. *Biophys J* 96:5040–5049.
57. Leach J, et al. (2009) Comparison of Faxén's correction for a microsphere translating or rotating near a surface. *Phys Rev E Stat Nonlin Soft Matter Phys* 79:026301.
58. Storath M, Weinmann A (2014) Fast partitioning of vector-valued images. *SIAM J Imaging Sci* 7:1826–1852.
59. Yuan J, Berg HC (2008) Resurrection of the flagellar rotary motor near zero load. *Proc Natl Acad Sci USA* 105:1182–1185.
60. Block SM, Berg HC (1984) Successive incorporation of force-generating units in the bacterial rotary motor. *Nature* 309:470–472.
61. Yonekura K, Maki-Yonekura S, Homma M (2011) Structure of the flagellar motor protein complex pomab: Implications for the torque-generating conformation. *J Bacteriol* 193:3863–3870.
62. Hales T, et al. (2017) Formal proof of the Kepler conjecture. *Forum Mathemat Pi* 5:e2.

Supporting Information

Nord et al. 10.1073/pnas.1716002114

SI Materials and Methods

Bacteria and Experimental Configuration. We use *E. coli* strain MTB32, a derivative of RP437. In MTB32, *FlgE*, the gene expressing the hook, is replaced with an Avidity tagged peptide fused *FlgE* for conjugation of biotin (27). Additionally, we genetically delete *CheY*, the chemotactic response regulator, via Red/ET recombination (Gene Bridges). Frozen aliquots of cells (100 μL, grown to saturation and stored in 25% glycerol at −80 °C) are grown in Terrific Broth (Sigma-Aldrich) at 33 °C for 5 h, shaking at 200 rpm. The final OD_{600} is 0.5–0.6. Cells are immobilized to a poly-L-lysine (Sigma-Aldrich; catalog no. P4707)-coated coverslip (Menzel-Gläser) in custom-made flow slides. Streptavidin superparamagnetic beads (1.36 μm, Sigma-Aldrich; 543 or 302 nm, Adamtech) are washed in PBS (Sigma-Aldrich), resuspended in motility buffer (10 mM potassium phosphate, 0.1 mM EDTA, and 10 mM lactic acid, pH 7.0), and then allowed to spontaneously attach to the biotinylated hooks. Experiments are performed in motility buffer at 22 °C. The sample is illuminated by using a 660-nm laser diode (Onset Electro-Optics; catalog no. HL6545MG) on a custom-built inverted microscope. The hologram of rotating beads is imaged via a 100 × 1.45-NA objective (Nikon) onto a CMOS camera (Optronics CL600x2/M) at 1,000 Hz. The x, y position of the rotating bead is determined by using cross-correlation analysis of the bead image (28, 55). Beads attached directly to the poly-L-lysine are used as fiducial markers for drift correction. An ellipse is fit to the drift-corrected x, y positions to yield the angular positions. Ellipses are transformed to circles under the assumption that the observed elliptical trajectories are a projection of a tilted circle. An example trajectory is shown in Fig. 1 *B*, *Inset*. The resulting angle and speed traces are median-filtered by using a window of 0.5 s. All analysis is performed with custom LabView, Python, and MATLAB scripts. Two magnets (aligned antiparallel, NdFeB, Supermagnete) (56) are mounted above the sample plane onto a linear motor (Standa), which controls the distance between the magnets and the sample plane. Full movement of the motor is achieved in <3 s.

Motor Torque Calculation and Fitting. The rotational viscous drag coefficient of a bead bound to the hook of a functional BFM is calculated as

$$\gamma = \frac{8\pi\eta r_b^3}{1-(1/8)(r_b/d)^3} + \frac{6\pi\eta r_e^2 r_b}{1-(9/16)(r_b/d)+(1/8)(r_b/d)^3} \quad \textbf{[S1]}$$

where η is the viscosity of the surrounding buffer, r_b is the radius of the bead, r_e is the measured radial distance to the bead's axis of rotation, and d is the distance from the bead to the cell surface, estimated to be 5 nm in our experiments. In Eq. **S1**, the denominator corresponds to Faxen's corrections (57). The torque which the motor applies upon the viscous load of the bead is $\tau_{motor} = \gamma\omega$, where ω is the measured bead's rotational velocity.

Torque traces are assumed to be noisy piecewise constant signals. A minimization of the L^1-Potts functional is used to recover the underlying piecewise constant torque signal for both the prestall and poststall motor torque traces. This is done via the PottsLab toolbox (Version 0.42) in Matlab (31, 58). An example torque trace and its fit is shown in Fig. 1*C*. This algorithm is ideal, as it allows for the identification of discrete discontinuities, or steps, in the torque signal, while not requiring them to be of any specific size or the same size.

Stator Stoichiometry Calculation and Analysis. Stator stoichiometry is determined by preserving the discrete discontinuities from the step-detection algorithm. As in previous works, the steps found in the torque traces are interpreted as indications of a change in stator number (11, 13, 14, 59, 60). For each individual motor, the average step size is used to determine the stator number as a function of time (see below for more details and a test of both the step detection and stator stoichiometry determination algorithms).

Kernel density estimate distributions (Fig. 2 *A*, *B*, and *D*) are constructed with a Gaussian kernel (width of 1/2 the SD of all fit torque steps in Fig. 2*A*; width of 1 stator in Fig. 2 *B* and *D*). Average single-stator torque values are determined by performing a two-Gaussian fit to these distributions, where only the mean m_1 and SD s_1 of the first Gaussian are free parameters, while the second Gaussian mean is set to $m_2 = 2m_1$ and the SD is set to $s_2 = \sqrt{2}s_1$. This considers large torque discontinuities as unresolved double steps, and allows to better fit the long tail of the distribution. Single-stator local force values (Fig. 3 *B*–*D*) are calculated as the average single-stator torque divided by the radius of the rotor [23 nm (42)].

For each viscous load except γ_{1300} (in which stall has no statistical effect on the motor), Eq. **3** is fit to the average stoichiometry data after stall, with k_{in}, k_{off}, N_{ss}, and N_o left as free parameters (least-squares minimization, black dashed line for $t > 0$ in Fig. 2*D*). From the distributions of N at steady-state shown in Fig. 2*B* (and considering the uncertainty of these measurements), in this analysis we fix $N_{max} = 14$, which is compatible with previous estimates of 11–16 (10, 14–16, 60). However, our main conclusions do not critically depend on this choice. The errors of the fit parameters shown in Fig. 3 *A* and *B* are estimated by bootstrapping, using the SD of the set of parameters that fit 100 random subsamples (each containing 90% of the original set of traces) for each viscous load. To quantify the rates at γ_{1300}, given the relatively constant value of k_{on} for the smaller viscous loads, we make the assumption that $k_{on}(\gamma_{1300})$ is equal to the average of k_{on} for the smaller viscous loads. From the value of $N_{ss}(\gamma_{1300})$, we then obtain $k_{off}(\gamma_{1300})$ from Eq. **S2** (points in cyan in Fig. 3 *A* and *B*).

In addition to the Hill–Langmuir adsorption model described by Eq. **3**, we also consider a generalized reversible RSA model which incorporates a continuous binding ring around the rotor. As this model does not have an analytical solution, we determine stator binding and unbinding rates using a genetic algorithm (differential evolution) to match simulated stator stoichiometry time trajectories to the average of the experimental trajectories. See below for details.

A Subset of Experimental Traces. Motor torque is recorded for a total of 142 motors, both before and after motor stall via the magnetic tweezers. All of the data are fit to a piecewise constant signal. A subset of experimental traces is shown in Fig. S1.

Detecting Steps in the Torque Traces. Torque traces are assumed to be piecewise constant signals with Gaussian noise. A minimization of the L^1-Potts functional is used to recover the underlying piecewise constant torque signal, $\tau_{fit}(t)$ (in units of pN·nm). This is done via the PottsLab toolbox (Version 0.42) in Matlab (30, 31). Torque traces are median-filtered by using a window of 0.5 s, then down-sampled to 10 Hz to decrease computation time. The number of steps detected is sensitive to one free parameter, which can be thought of as a smoothing parameter. Ideally, this parameter should be set such that the fit contains the

smallest number of steps where the residuals contain no trace of the underlying signal (i.e., the residuals are pure noise). This is accomplished by performing multiple fits of the data, varying the parameter over a wide range, and fitting a Gaussian function to the residuals. The optimal parameter value is chosen as the lowest value for which increasing the paramter value yields no improvement of the residual fit, as judged by the Bayesian information criterion.

Determining Stoichiometry. Starting from the piece-wise constant fit $\tau_{fit}(t)$ (in units of pN·nm) for each of the motor torque traces, stator stoichiometry is determined in the following way.

1. The global mean step size is determined for each load from a double-Gaussian fit of the distributions shown in Fig. 2*A*. This global value is assumed to be the torque contribution of a single stator at the load γ, $\mathcal{T}_{SS}(\gamma)$.
2. To account for the possibility of cell-to-cell variation, the torque contribution due to a single stator is estimated for each individual motor. For each motor, using $\tau_{fit}(t)$ from both before and after stall, all of the torque discontinuities $\{\delta\tau_i\}$ in the range $\frac{1}{2}\mathcal{T}_{SS}(\gamma) < \delta\tau_i < 3\,\mathcal{T}_{SS}(\gamma)$ are averaged to give the single-stator torque contribution of the individual motor $\tau_{SS} = \langle\{\delta\tau_i\}\rangle$. For an individual trace, this step is implemented to reduce the effect of discontinuities which represented multiple stators binding or unbinding simultaneously (or within the time resolution of the fit, see below) or pauses in motor rotation due to surface interactions or other unknown causes.
3. The stator number N at time t is reconstructed as follows. $N(t = 0)$ is initially set to zero. Moving forward along the trace $\tau_{fit}(t)$, $N(t)$ remains unchanged until a discontinuity $\delta\tau_i$ in the fit is encountered at $t = t_o$.

- If $\delta\tau_i < \frac{1}{3}\tau_{SS}$, the discontinuity is assumed to be too small to represent a change in stator number and $N(t_o)$ is unchanged.
- If the discontinuity is in the range $\frac{1}{3}\tau_{SS} \leq \delta\tau_i < \frac{3}{2}\tau_{SS}$, the discontinuity is interpreted as the arrival or departure of a single stator, and N is changed accordingly [i.e., $N(t_o) = N(t_o - \Delta t) \pm 1$, where Δt is the sampling time].
- For discontinuities $\delta\tau_i > \frac{3}{2}\tau_{SS}$, two or more stators are assumed to have bound or unbound, and N is changed accordingly [i.e., $N(t_o) = N(t_o - \Delta t) \pm \Delta N$, with ΔN the nearest integer to $\delta\tau_i/\tau_{SS}$].

This procedure produces a trace of a relative $N(t)$ which accurately reflects the sizes and positions of the discontinuities of the traces, but does not yet accurately reflect the absolute stator number, as $N(t = 0)$ is a priori unknown.

4. In the trace $\tau_{fit}(t)$, close but different torque values can correspond to the same relative number of stators, according to the reconstructed $N(t)$. All of the torque values of $\tau_{fit}(t)$ that correspond to the same $N(t)$ are averaged together, obtaining $\langle\tau_N\rangle$, the average motor torque at the (relative) stator number N.
5. To offset the relative trace $N(t)$ to most accurately reflect the real stator number, the following global offset is added

$$N(t) \rightarrow N(t) + rint\left(\left\langle \frac{\langle\tau_N\rangle}{\tau_{SS}} - N(t)\right\rangle\right) \qquad \textbf{[S2]}$$

where $rint(x)$ is the closest integer to x.

Evaluation of Step Finding and Stoichiometry Algorithms. To test the step detection and stoichiometry assignment algorithms, simulated BFM torque traces are created and analyzed. Two different types of artificial traces are created, both assuming that the torque of the BFM is piecewise-constant with Gaussian noise. The first type of artificial trace incorporates 10 discrete discontinuities, 5 upward and 5 downward, an example of which is shown in Fig. S2*A*. The torque trace is defined here by a piecewise-constant signal τ, to which a zero-mean delta-correlated Gaussian noise is added to simulate the high-frequency noise in each torque level. After applying a median filter (equivalently to the experimental traces), the amplitude of this torque noise is quantified as σ_τ. To simulate nonidentical torque steps induced by binding and unbinding of a single stator, each of the torque discontinuities in the trace is defined by a step size $\delta\tau$ (constant in absolute value), to which a random number (extracted from a normal distribution with SD $\sigma_{\delta\tau}$) is added. The second type of simulated trace incorporates 20 brief discontinuities in the form of pulses, with an increasing duration δt of the pulse (refer to the purple arrow in Fig. S2*B*), an example of which is shown in Fig. S2*B*.

Two parameters are varied in the simulations: the SD in the discontinuity size (quoted as a percentage of the discontinuity size, $\sigma_{\delta\tau}/\delta\tau$; refer to the green arrow in Fig. S2*A*) and the Gaussian noise added to the torque trace (as measured after median filtering and quoted as a percentage of the discontinuity size, $\sigma_\tau/\delta\tau$; refer to the blue arrow in Fig. S2*A*). Fifteen simulated traces are created for each condition and for each type of artificial trace, for a total of 1,050 simulated traces. The time resolution and the median filtering of the traces match that of the experimental traces.

Fig. S2 *A* and *B* shows examples of the two types of artificial traces with the lowest values of $\sigma_\tau/\delta\tau$ and $\sigma_{\delta\tau}/\delta\tau$ tested, after median filtering. Fig. S4 *E* and *L* shows examples for the highest values of $\sigma_\tau/\delta\tau$ and $\sigma_{\delta\tau}/\delta\tau$. While Fig. S2 *G*, *H*, *K*, and *L* shows good overall recovery of the underlying torque signal and stator number; Fig. S2 *E*, *F*, *I*, and *J* shows poor recovery, highlighting situations under which the algorithms fail. Fig. S2 *C* and *D* shows results of the average error in the stator stoichiometry determination for all of the simulations.

Evaluating all of the experimental traces of this study, we estimate the experimental SD in step size $\sigma_{\delta\tau}$ to be in average 0.5 times the experimental step size $\delta\tau$ over all three loads, and the experimental SD of the noise in the torque traces σ_τ to be 0.4 times the experimental step size $\delta\tau$. Based upon these estimates and the results of the simulations shown in Fig. S2 *C* and *D*, we estimate the error in stator stoichiometry to be ± 1.6 stators. In addition, for the above-mentioned values of experimental noise, simulations of the type shown in Fig. S2*B* suggest that steps in motor torque of duration <3.5 s are detected by our algorithms 50% of the time, while steps that last 4.0 s are detected 67% of the time.

Simulations of a Reversible RSA Model with a Continuous Binding Ring. While the Hill–Langmuir model proposed in Eq. **3** fits the experimental data well, we note that fixed binding sites within the PG may not be biologically likely. Therefore, we explore how stator kinetics differ if the model is generalized to a continuous binding ring at the periphery of the rotor (see Fig. S4 *A* and *B* for a schematic comparison of the two models). As this model lacks an analytical solution, we perform stochastic simulations of the binding and unbinding events, varying the free parameters of Eq. **3**, and compare these to experimental traces.

Stators are allowed to bind at any continuous angle on the ring providing there is sufficient contiguous space. The perimeter of the ring is set to $d \cdot N_{max}$, where the stator is assumed to be a sphere of diameter d. The reaction of stator unbinding is identical to the Hill–Langmuir model, dependent upon k_{off} and the number of stators currently bound. The comparison between simulated trajectories and experimental trajectories is accomplished by using a genetic algorithm (differential evolution) to minimize a score function that measures the square distance between the experimental occupancy trajectory $\langle N(t)\rangle$ and the average of 2,000 stochastic simulated trajectories for each parameter set. A continuous binding ring results in lower steady-state occupation than its discrete Hill–Langmuir version,

due to "frustration" effects in stator packing efficiency [previously, it has been shown that the irreversible packing limit is 0.74 (62)]. The relative size of the stator to the continuous binding ring which produces a good fit of the experimental data equates to a maximum number of fixed binding sites, N_{max}, of 20. The 3D structure of the stator unit of PomAB in *Vibrio alginolyticus* has a cross-section of ∼8 nm (61). Neglecting interactions between stator units, ∼21 stator units could attach to the PG at a radius of 27 nm [23-nm rotor radius (42) plus 4-nm stator radius]. Fig. S4C shows the data from Fig. 3 for each load which could be fit with Eq. **3**, as well as the equivalent rates as determined by using the reversible RSA model with a continuous binding ring.

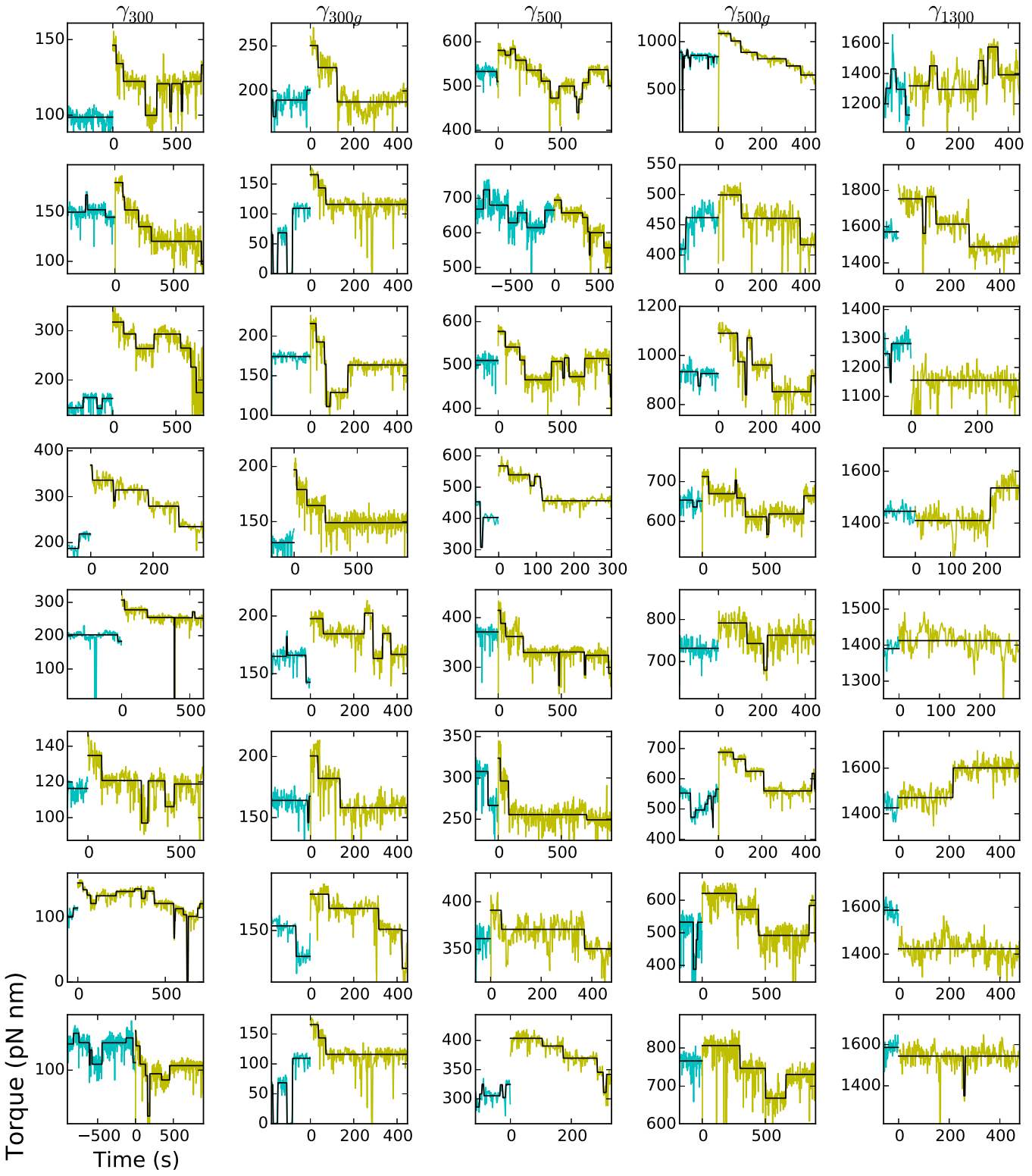

Fig. S1. A collection of experimental torque traces. The five columns refer to the five loads γ_{300}, γ_{300g}, γ_{500}, γ_{500g}, and γ_{1300}. Torque is measured at steady state before stall (cyan points, $t < 0$). After being stalled for 5 min, the motor is released, and torque is measured again (yellow points, $t > 0$). The black line shows the result of the piece-wise constant fit, later used to estimate the stoichiometry of stators along each trace.

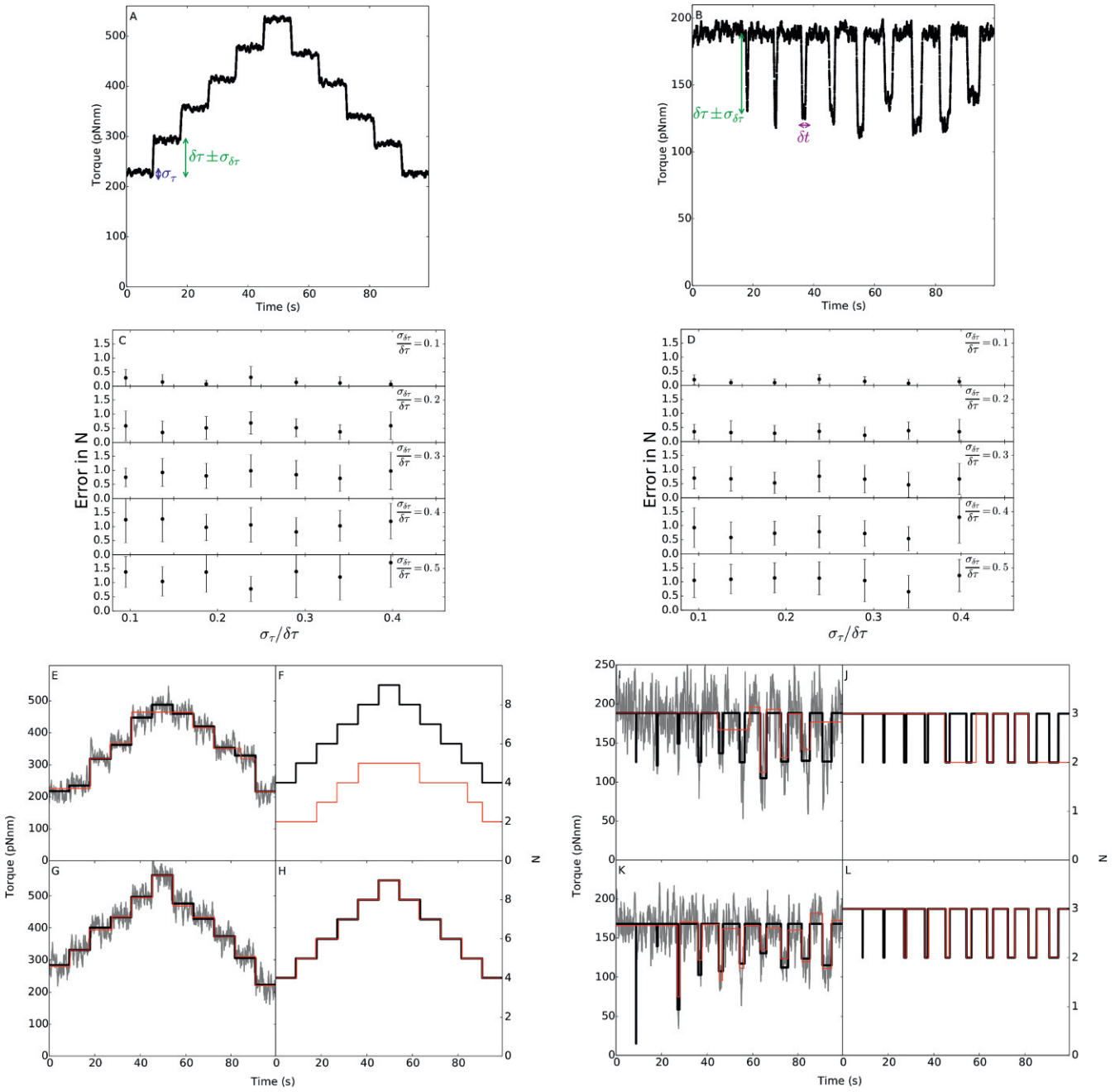

Fig. S2. Simulations to evaluate the step detection and stator stoichiometry determination algorithms. (*A* and *B*) Examples of the two types of simulated traces used to evaluate the algorithms. These traces represent the lowest values of $\sigma_\tau/\delta\tau$ and $\sigma_{\delta\tau}/\delta\tau$ tested. An average step size of 61 pN·nm is shown here, similar to loads γ_{1300}. (*C* and *D*) The error in the determination of stator stoichiometry for the types of traces shown in *A* and *B*, respectively. Each point represents the average of 15 simulated traces, with the error bars showing SD. *E*, *G*, *I*, and *K* show simulated traces representing the highest values of $\sigma_\tau/\delta\tau$ and $\sigma_{\delta\tau}/\delta\tau$ tested. The black line represents the simulated motor torque before the addition of Gaussian noise, the gray line represents the simulated motor torque after addition of Gaussian noise, and the red line shows the best fit from the step-detection algorithm. Examples of poor performance by the step-finding algorithms is shown in *E* and *I*, whereas examples of good performance are shown in *G* and *K*. *F*, *H*, *J*, and *L* show the output of the stator stoichiometry algorithm for *E*, *G*, *I*, and *K*, respectively. The black line represents the simulated stator number, and the red line shows the stator number determined from the output of the step detection algorithm.

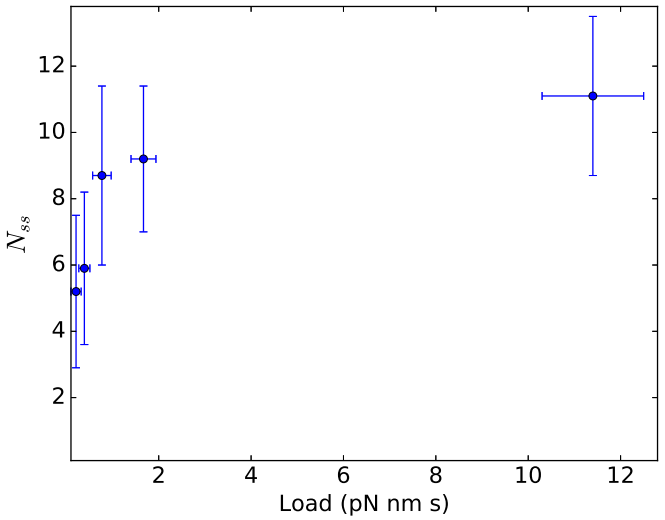

Fig. S3. Steady-state stator number, N_{ss}, as a function of viscous load. Dots and error bars represent averages and standard deviations, respectively, over all of the acquired data.

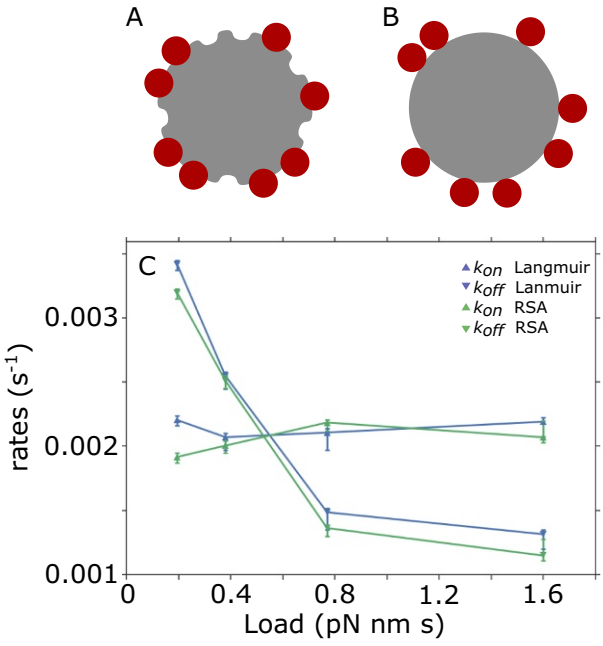

Fig. S4. A comparison of stator binding models presented in this work. (*A*) A schematic of the Hill–Langmuir model, where the number of stator binding sites, N_{max}, is 14. (*B*) A schematic of the continuous-binding ring RSA model, where perfect packing allows for 20 attached stators (N_{max} = 20), but excluded-volume effects impact stator occupancy. In *A* and *B*, the rotor and stators are shown in gray and red, respectively. (*C*) Rate constants extracted from experimental data using the Hill–Langmuir model described in the main text (blue; N_{max} = 14), and the reversible RSA model with a continuous binding ring (green; N_{max} = 20).

Table S1. Data were acquired for motors driving five different viscous loads, which were obtained by using beads of three different diameters and two buffer solutions of different viscosity

Symbol	Bead diam., nm	Glycerol	Drag, mean ± SD, pN·nm·s
γ_{1300}	1364 ± 98	0	11.4 ± 1.1
γ_{500g}	543 ± 148	25%	1.67 ± 0.27
γ_{500}	543 ± 148	0	0.77 ± 0.20
γ_{300g}	302 ± 40	25%	0.39 ± 0.12
γ_{300}	302 ± 40	0	0.21 ± 0.11

The loads are labeled γ_d or γ_{dg}, where *d* corresponds to the bead diameter (bead diam.), and *g* corresponds to the use of glycerol in the percent by volume listed. The corresponding calculated angular drag coefficients are given, and the bead diameters were measured by scanning electron microscopy.